Ultra-Low Concentration Gel Polymer Electrolytes Realize Stable and Low-Temperature Lithium−Organic Batteries

Mengjie Li[a,b], Hang Liu[a], Hai Su[a], Zehui Fan[a], Yuansheng Liu[a], Jixing Yang [a], Wei Zhu[a], Qinghao Chen[a] and Yunhua Xu[a]**

[a]School of Materials Science and Engineering, and Key Laboratory of Advanced Ceramics and Machining Technology (Ministry of Education), Tianjin University, Tianjin 300072, China.

[b]Institute of Technology for Carbon Neutrality, Shenzhen Institutes of Advanced Technology, Chinese Academy of Sciences, Shenzhen 518055, China.

Experiment Section

Materials: Battery-grade lithium bis(trifluoromethanesulfonyl) imide (LiTFSI), 1,3-dioxolane (DOL) and dimethoxyethane (DME) were purchased from Suzhou DuoDuo Chemical Technology Co., Ltd. $LiFePO_4$ (LFP) power, Li foils and PP separator were provided by Guangdong Canrd New Energy Technology Co., Ltd. Nafion D520 solution (5 wt% in a mixture of lower aliphatic alcohols and water) was obtained from Dupont Co. Commercial $Li_4Ti_5O_{12}$ (LTO) electrodes were purchased from Shenzhen Kejing Star Technology Co.,.

Electrodes/Electrolytes Preparation and Cell Assembly: The synthesis of the 1,3,5-tri(9,10-anthraquinonyl)benzene (TAQB) electrode material and the preparation of the gel polymer electrolyte initiated by Nafion could refer to our previous work.[1] Key experimental parameters are summarized as follows: Nafion D520 solution was coated on a PP separator and dried sequentially at room temperature for 1 h and at 60 °C for 6 h, followed by vacuum drying at 60 °C for 24 h. The resulting Nafion-coated separator, with a coating thickness of approximately 3 μm, was then used to initiate the *in situ* gelation of a DOL-based electrolyte (LiTFSI in DOL-DME) and the gelation process was conducted for 16 h. TAQB and LFP electrodes were prepared by mixing TAQB (or LFP), graphene, and polyvinylidene fluoride (PVDF) at a weight ratio of 6:3:1 in N-methyl-pyrrolidone (NMP) to form a uniform slurry. Then, the slurry was smeared on a carbon-coated aluminum foil and the NMP was evaporated at 60 °C for 6 h followed by vacuum drying at 80 °C for 24 h. The mass

loading of TAQB (or LFP) is about 0.8~1.2 mg cm^{-2}. For TAQB electrodes with high mass loading, polytetrafluoroethylene (PTFE) is used as the binder and steel mesh is used as the current collector, corresponding to an active material loading of about 8 mg cm^{-2}. CR2032-type coin cells were assembled in an Ar-filled glove box using Li foil as the anode, LiTFSI in DOL/DME (1/1, in volume) with different salt concentrations as the electrolyte, and Nafion-coated PP as the separator.

Material Characterizations: The morphology of the cycled electrodes and separators was observed by SEM (S-4800, Hitachi). The surface composition of the cycled Li anode was analyzed by X-ray photoelectron spectroscopy (XPS) (ESCALAB 250, Thermo-VG) system. ^{1}H NMR spectra (AVANCE III 400 MHz, Bruker) was used to verify the polymerization of DOL with $CDCl_3$ as the deuterated solvent. Gel permeation chromatography (GPC) (PL-GPC50) was conducted to demonstrate the number-average molecular weight (Mn) of the synthesized Poly-DOL (PDOL).

Electrochemical Measurements: Cyclic voltammetry (CV), electrochemical impedance spectroscopy (EIS) and the Li-ion transference number (t_{Li^+}) tests were performed on Solartron Analytical 1470 (AMETEK, USA). The CV curves were scanned at different scan rates with the voltage window of 1.5 to 3.0 V for TAQB and 2.7 to 4.0 V for LFP, respectively. For EIS test, the frequency range was from 1×10^6 to 0.1 Hz with the voltage amplitude of 5 mV. The ionic conductivity of the electrolyte was obtained in symmetrical stainless steel (SS) electrodes by the following equation:

$$\sigma=\frac{L}{R_b\times S} \tag{1}$$

where L and S are corresponding to the thickness and contact area of the separator, R is the bulk resistance of the SS-SS cells.

The t_{Li^+} of the electrolyte was evaluated by the steady-state current method using symmetric Li-Li cells, which was calculated using the following equation:

$$t_{Li^+}=\frac{I^s(\Delta V-I^0R^0)}{I^0(\Delta V-I^SR^S)} \tag{2}$$

where ΔV is the applied polarization voltage (10 mV), I^0 and I^s are the initial and stable currents during polarization process, while R^0 and R^s are the charge-transfer resistances of Li-Li cells before and after the polarization respectively.

The Li-ion diffusion coefficient (D_{Li^+}) is calculated by CV and galvanostatic intermittent titration technique (GITT) measurements respectively. From the Randles-Sevcik equation, the D_{Li^+} could be calculated according to the CV curve of electrode material at different scanning rates:

$$I_p = 2.69\times10^5 n^{1.5} A D_{Li^+}{}^{0.5} C_{Li} v^{0.5} \quad (3)$$

where I_p is the peak current in the CV curves, n is the electron transference number, A is the surface area of the electrode, D_{Li^+} is the diffusion coefficient of Li ions, C_{Li} is the Li^+ concentration in the electrode material and v is the scan rate.

For the GITT measurements, the cells were charged or discharged at a current pulse of 0.1 C for 30 min, followed by open circuit relaxation for 4 h. The procedure was continued until the voltage of the cells reached a preset value. The Li-ion diffusion coefficient (D_{Li^+}) according to GITT was calculated based on the following equation:

$$D_{Li^+} = \frac{4}{\pi\tau}\left(\frac{m_b V_m}{M_B S}\right)^2\left(\frac{\Delta E_s}{\Delta E_t}\right)^2 \quad (4)$$

where τ is the constant current pulse time; m_b, V_m, M_B, and S are the mass loading of the active material, molar volume, molecular weight, and the area of the electrode-electrolyte interface, respectively; ΔE_s is the voltage difference between the steady state and the initial state of every step; and ΔE_t is the change of total voltage during a pulse step excluding the IR drop.

The experimental determination of the desolvation energy was achieved by EIS measurements of symmetrical Li cells at various temperatures based on the following equation:

$$\frac{1}{R_{desolvation}} = A\exp\left(-\frac{E_{desolvation}}{RT}\right) \quad (5)$$

where $R_{desolvation}$ is the charge transfer resistance of symmetrical Li cells; $E_{desolvation}$ is the activation energy of desolvation; A, R and T are the pre-exponential constant, standard gas constant and the absolute temperature, respectively.

The rate capability and cycling performance of all batteries were performed on a Neware battery testing system (CT-4008T).

Theoretical Simulations and Analysis: All the all-atom molecular dynamics (MD) simulations were based on a general AMBER force field[2] with the RESP charges[3] and were carried out using the Gromacs-2022 software package.[4] The simulation systems were composed of 962 DME, 286 DOL, 112 PDOL long chain (the number of repeating unit of -C-C-O-C-O- is 10) and a certain amount of Li^+ and $TFSI^-$ to reach LiTFSI concentrations of 0.1 M and 1.0 M. For the 0.1 and 1.0 M GPEs, simulations were conducted with 20 and 200 LiTFSI molecules, respectively. The system is a relaxed liquid configuration at 223.15 K and 298.15 K. The total run time was 20 ns NPT for the equilibrium MD simulation. We used the relaxed system as a starting configuration. As it is prior to system relaxation MD, energy minimization was carried out with a composite protocol of steepest descent using termination gradients of 500 kJ mol^{-1} nm^{-1}. The Nose´-Hoover thermostat[5] was used to maintain the equilibrium temperature at 223.15 K and 298.15 K and periodic boundary conditions were imposed on all three dimensions. The Particle Mesh-Ewald method[6,7] was used to compute long-range electrostatics within a relative tolerance of 1×10^{-6}. A cut-off distance of 1nm was applied to real-space Ewald interactions. The same value was used for van der Waals interactions. The LINCS algorithm[8] was applied to constrain bond lengths of hydrogen atoms. A leap-frog algorithm[9] was used with a time step of 2 fs.

The solvation states of Li^+ in GPEs was obtained by analyzing the trajectory of MD simulations. The de-solvation free energy of each solvation structure is obtained by quantum chemistry calculation, which was performed using Gaussian 16 software package. Geometry optimizations and energy calculations were performed using B3LYP-D3 functional and TZVP basis set, and vibration analysis is carried out to ensure the local minimum value is reached and to obtain the thermal correction to Gibbs free energy.

The single point energy of the optimized structure was calculated by B2PLYP functional at def2-TZVP level of basis set. Assuming the solvation structure of LiA_xB_y, where A and B represent the solvent molecules around a Li^+, and x and y represent the number of solvent molecules in each solvation structure. The free energy of de-solvation for each solvation structure can be obtained by using the following equation:

$$\Delta G_{\mathrm{de-}solvation}\left(LiA_xB_y\right) = G_{gas}\left(Li^+\right) + xG_{solv}\left(A\right) + yG_{solv}\left(B\right) - G_{solv}\left(LiA_xB_y\right) \quad (6)$$

where G_{gas} and G_{solv} represent the Gibbs free energy of gaseous and solvation components, respectively. For the same structure, the difference between G_{solv} and G_{gas} is the free energy of solvation, which is obtained by deducting the electronic energy calculated using the SMD solvent model at M052X/6-31G* level from that calculated without the SMD solvent model.

The simulated trajectories in different Li^+ solvation structures were counted. Using the last 20 ns trajectories, 50 data simulation configurations were taken at equal intervals. The occurrence frequency of solvation structure was counted according to a radius of 0.3 nm around Li^+, and the de-solvation free energy of each solvation structure was calculated using weighted average method.

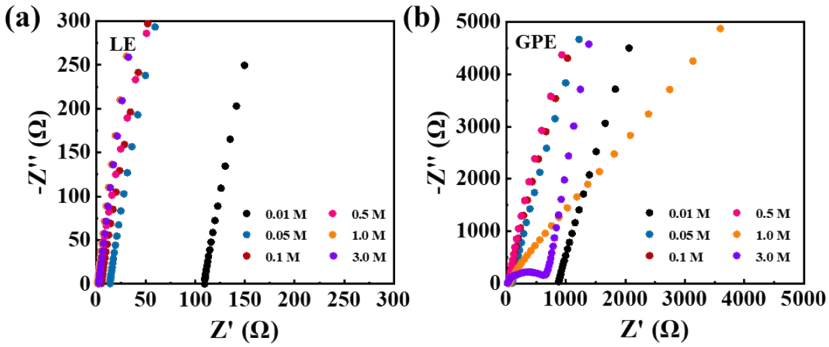

Figure S1. EIS spectra of symmetrical steel cells using (a) LEs and (b) GPEs with different LiTFSI concentrations from 0.01 to 3.0 M.

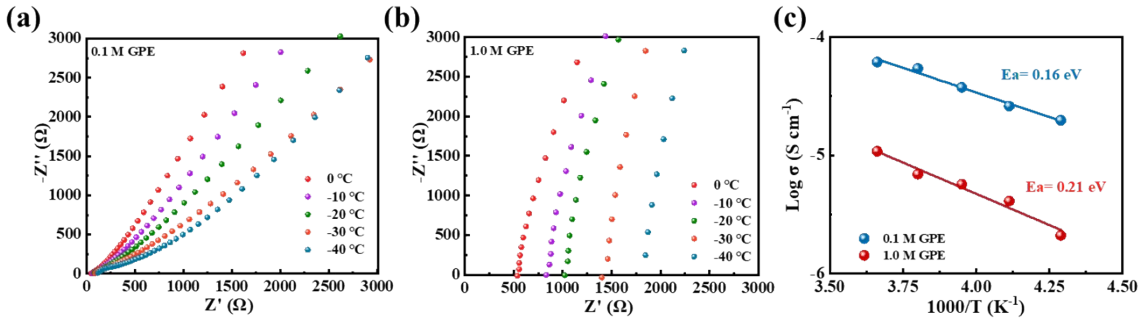

Figure S2. EIS spectra of symmetrical steel cells using (a) 0.1 and (b) 1.0 M GPEs at different temperatures. (c) Temperature dependence of the ionic conductivities of 0.1 and 1.0 M GPEs.

As shown in Figure S2, in contrast to the high bulk impedance of the 1.0 M GPE at low temperatures, the 0.1 M GPE exhibits lower impedance and higher ionic conductivity over the same temperature range. In addition, the 0.1 M GPE also exhibits a lower activation energy, indicating a reduced ion transport energy barrier in the electrolyte.

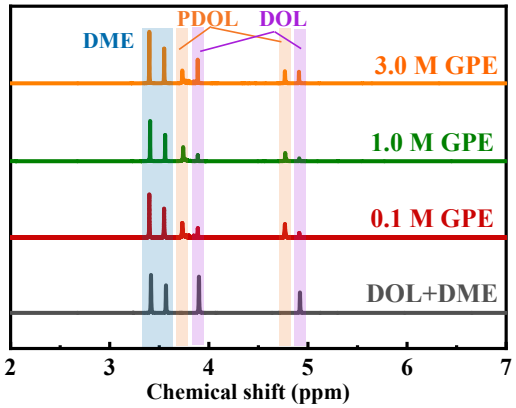

Figure S3. ^{1}H NMR spectra of GPEs with different LiTFSI concentrations from 0.1 to 3 M and the corresponding solvent.

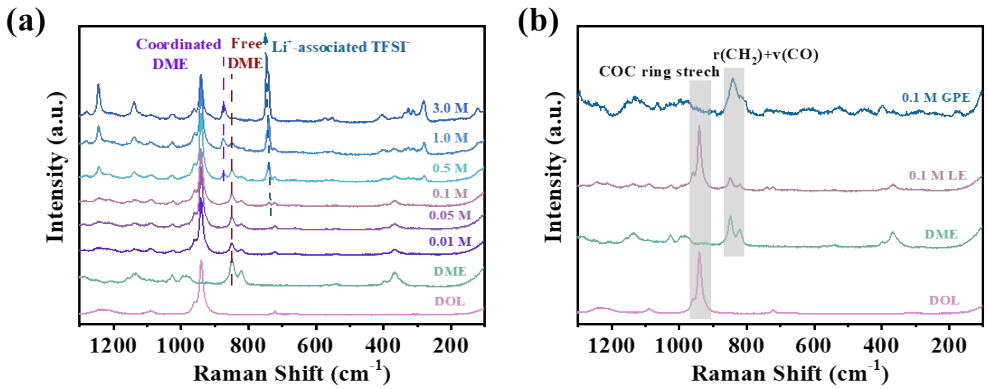

Figure S4. (a) Raman spectra of pure solvents and LEs with different salt concentrations; (b) Raman spectra of pure solvents, 0.1 M LE and 0.1 M GPE.

For the Raman shift from 800 to 900 cm^{-1}, two absorption bands at 820 and 848 cm^{-1} are attributed to the stretching vibration of $-CH_2-O-CH_3$ groups in free DME molecules (Figure S4). In liquid electrolytes, as the LiTFSI concentration increases to 3.0 M, the free DME gradually diminishes, forming Li^+-coordinated DME (874 cm^{-1}). Furthermore, with increasing salt concentration, the symmetric C–O–C stretching vibration peak of DOL at 939 cm^{-1} remained nearly unchanged, indicating that DOL molecules preferentially exist as free solvent species rather than coordinating with Li^+ in the solvation sheath due to the steric hindrance and the low electronegativity of oxygen atoms. Raman peaks in the range of 730 to 750 cm^{-1} are assigned to the formation of Li^+–$TFSI^-$ ion clusters and dissociated ions. As the LiTFSI concentration increases, the S–N–S vibrational peak of $TFSI^-$ shifts to higher wavenumbers, indicating enhanced formation of Li^+–$TFSI^-$ ion clusters. However, it is challenging to analyze the solvation structure of GPEs using Raman spectroscopy due to the overlapping peaks of PDOL and DME in the range of 800–900 cm^{-1}.

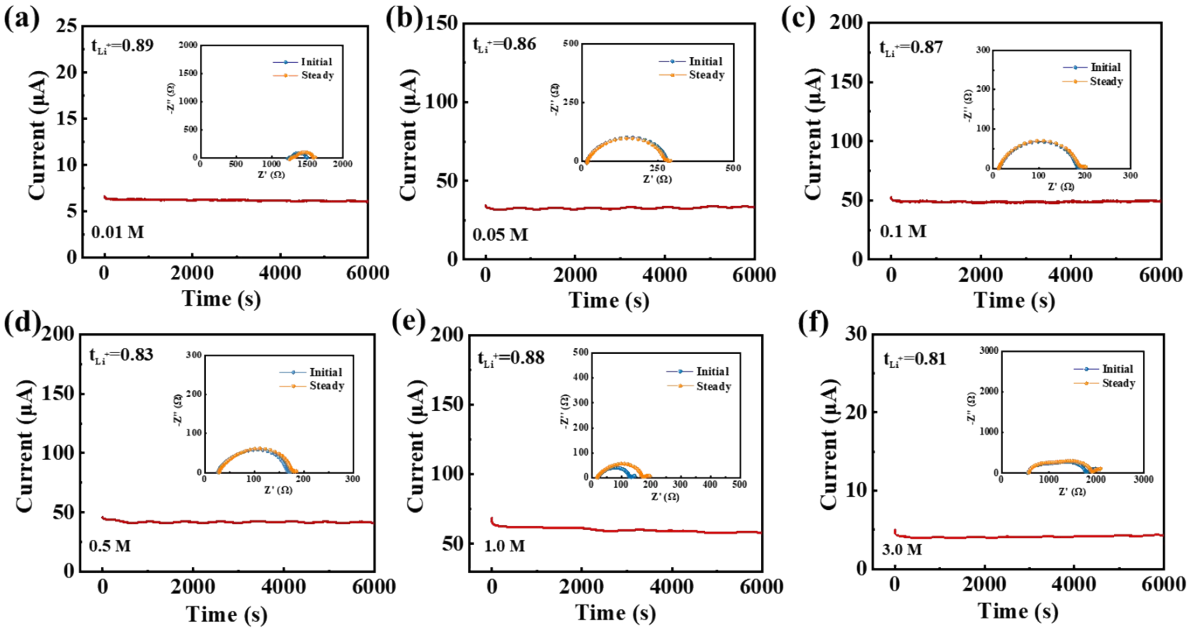

Figure S5. Chronoamperometry profiles of symmetrical Li cells using (a) 0.01, (b) 0.05, (c) 0.1, (d) 0.5, (e) 1.0 and (f) 3.0 M GPEs. Insets: the impedance spectra before and after polarization.

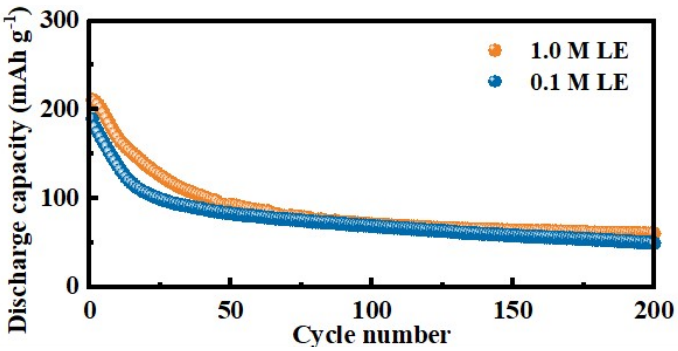

Figure S6. Cycling performance of TAQB-Li batteries using LEs with different LiTFSI concentrations of 0.1 and 1.0 M.

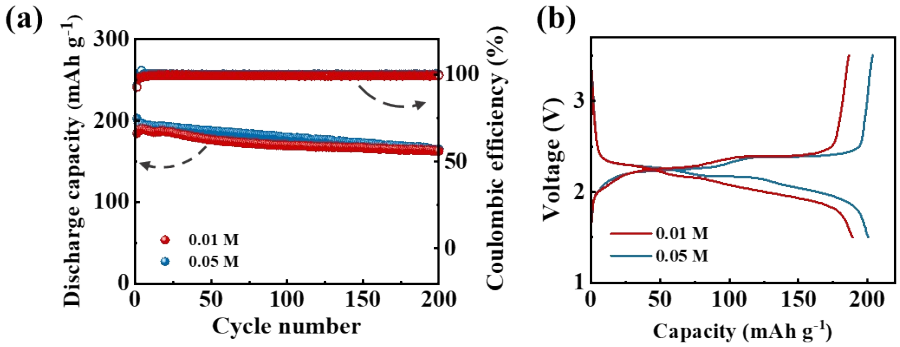

Figure S7. (a) Cycling performance and (b) corresponding charge-discharge curves of TAQB-Li batteries using GPEs with different LiTFSI concentrations of 0.01 and 0.05 M.

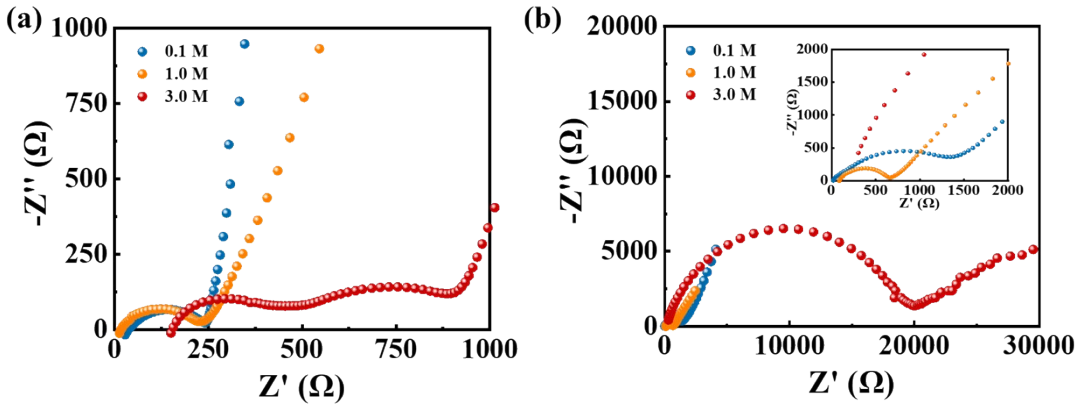

Figure S8. EIS patterns of (a) TAQB-Li and (b) LFP-Li batteries using 0.1, 1.0 and 3.0 M GPEs.

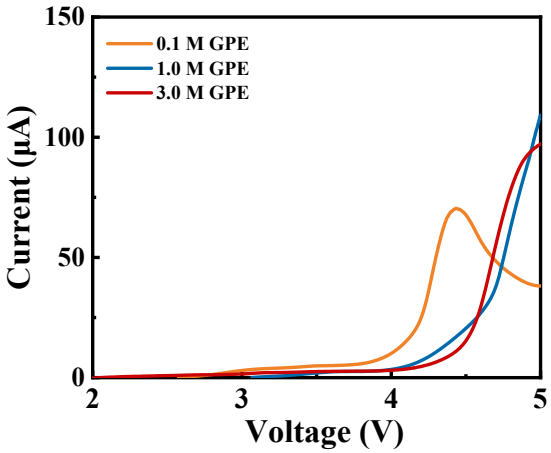

Figure S9. Electrochemical stability windows of GPEs with different salt concentrations.

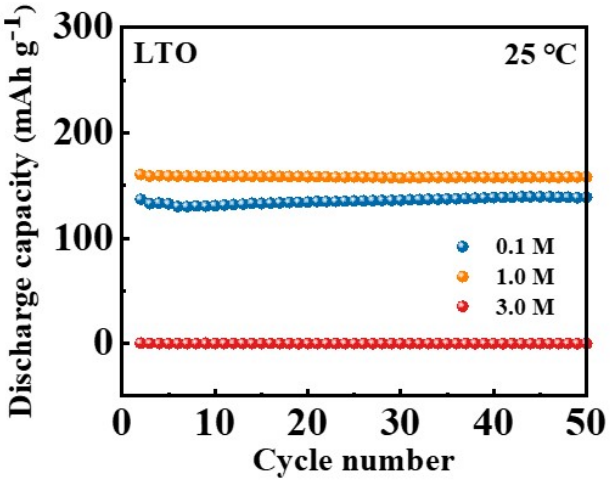

Figure S10. Cycling performance of LTO-Li batteries using GPEs with different salt concentrations within a voltage window of 1.0–2.5 V.

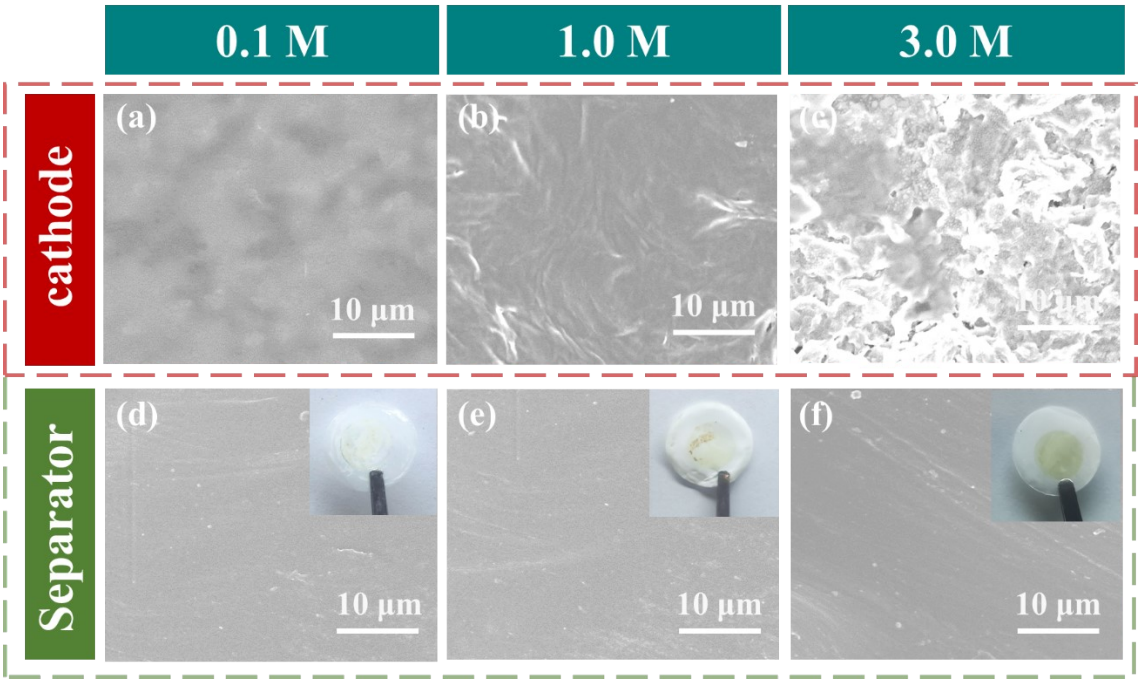

Figure S11. SEM images of (a-c) TAQB cathodes and (d-f) separators using (a,d) 0.1, (b,e) 1.0 and (c,f) 3.0 M GPEs after 200 cycles. Insets: corresponding photographs of separators.

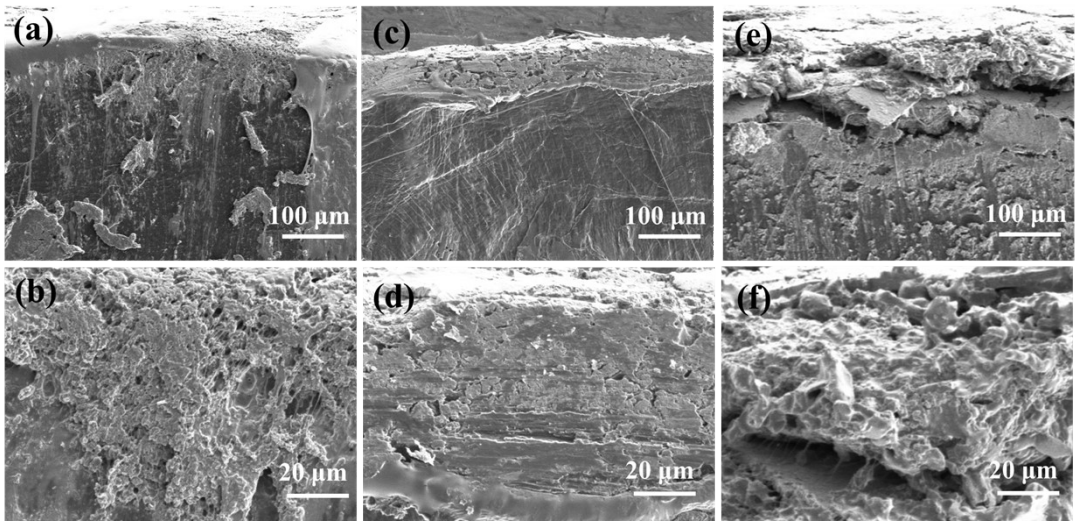

Figure S12. Cross-sectional SEM images of Li anodes cycled in 3.0 M GPEs after (a, b) 50, (c, d) 200 and (e, f) 500 cycles.

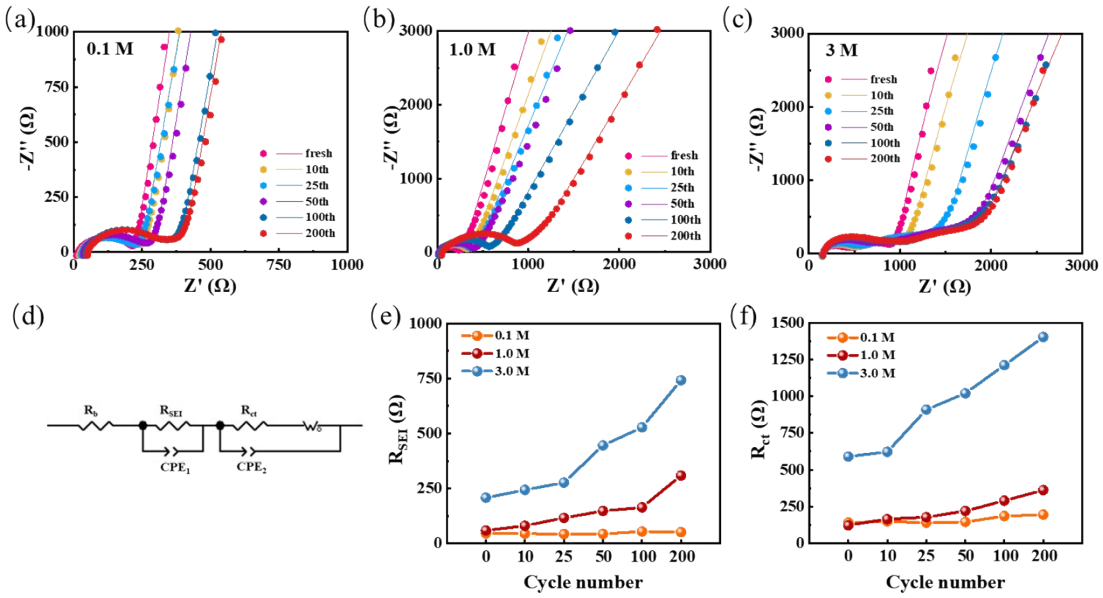

Figure S13. EIS changes of TAQB-Li cells within 200 cycles using (a) 0.1, (b) 1.0 and (c) 3.0 M GPEs. (d) The corresponding equivalent circuit for fitting. Changes of (e) the resistance across the solid electrolyte interphase (SEI) layer (R_{SEI}) and (f) charge-transfer resistance (R_{ct}) after different cycles.

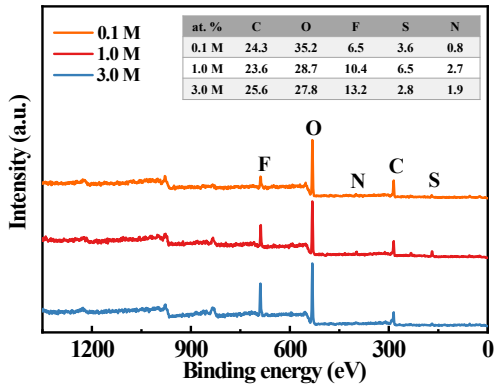

at. %	C	O	F	S	N
0.1 M	24.3	35.2	6.5	3.6	0.8
1.0 M	23.6	28.7	10.4	6.5	2.7
3.0 M	25.6	27.8	13.2	2.8	1.9

Figure S14. The total XPS spectra from the cycled Li anode with different concentrated GPEs, the inset table corresponds to atomic ration of elements.

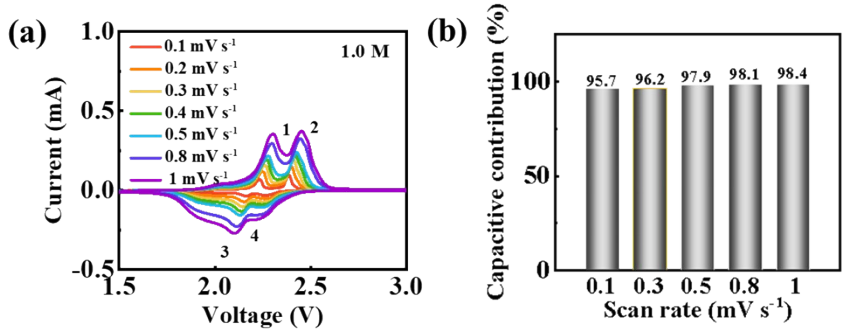

Figure S15. (a) CV curves and (b) the capacitive contributions of the TAQB electrode at different scan rates with 1.0 M GPE.

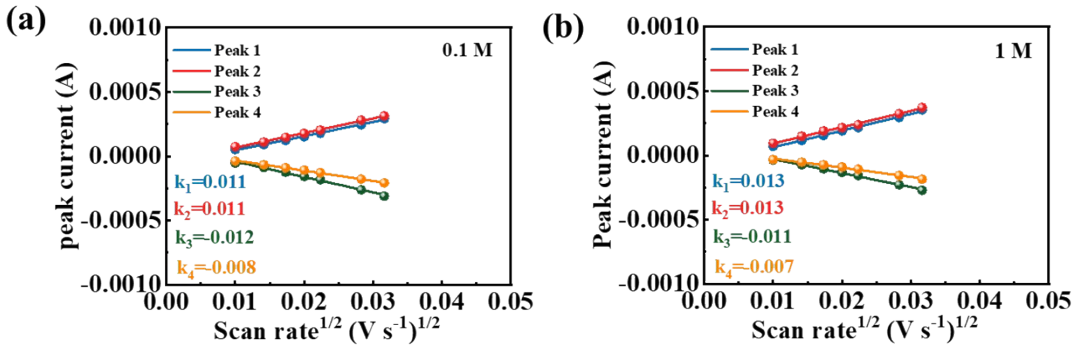

Figure S16. The relationships between the peak current and the square root of the scan rate of the TAQB-Li cells using (a) 0.1 and (b) 1.0 M GPEs based on CV curves recorded at different scan rates.

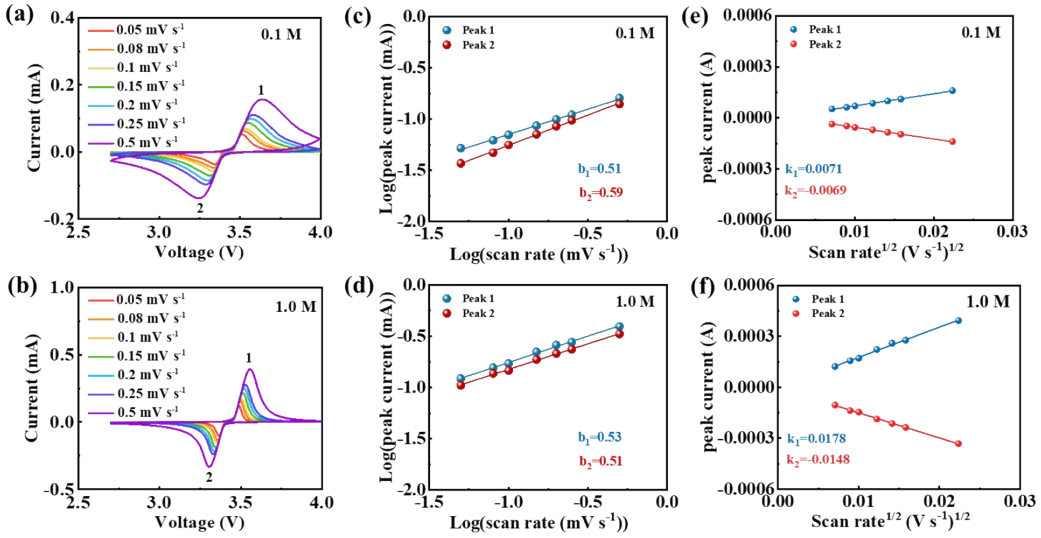

Figure S17 (a, b) CV curves of the LFP electrodes at different scan rates, (c, d) relationships between peak current and scan rate and (e, f) relationships between the peak current and the square root of the scan rate for the redox peaks using (a-c) 0.1 and (d-f) 1.0 M GPEs of the LFP-Li cells.

The relationship between peak current (i) and the scan rate (v) can be described by Equations 7 as follows:

$$i = av^b \quad (7)$$

A b-value approaching 0.5 indicates a diffusion-controlled mechanism, whereas a value near 1 suggests pseudocapacitive behavior. For LFP electrodes, the corresponding b values are close to 0.5 in both 0.1 and 1.0 M GPEs, indicating that the Li-storage behavior in LFP is mainly dominated by diffusion control, which is completely different from the fast capacitive-dominated Li-storage

process observed in TAQB electrodes.[10] The apparent chemical diffusion coefficients of Li ions (D_{Li^+}) can be calculated by Randles-Sevcik equation. In contrast to the similar D_{Li^+} values of TAQB using 0.1 and 1.0 M GPEs, the D_{Li^+} of the LFP electrode in 0.1 M GPE is nearly an order of magnitude lower than that in 1.0 M GPE (Figure S18).

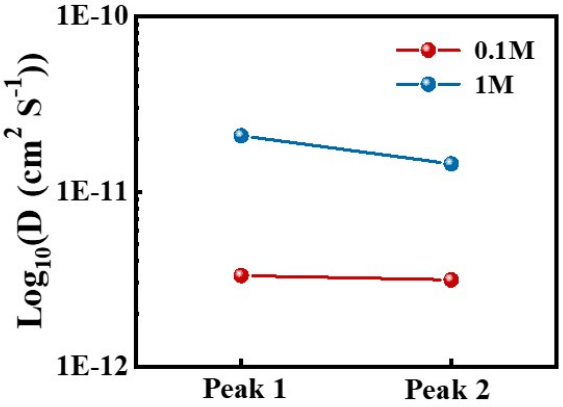

Figure S18. The Li-ion diffusion coefficients of the LFP electrode with 0.1 and 1 M GPEs based on Randles-Sevick equation.

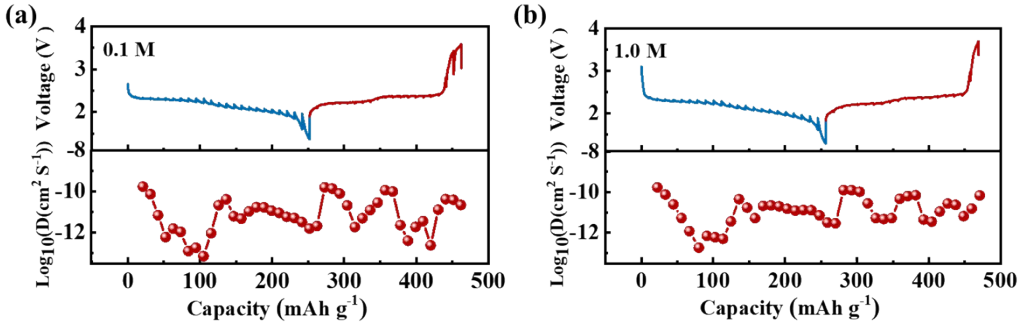

Figure S19 GITT curves of TAQB electrodes and the calculated Li-ion diffusion coefficients tested at 25 °C using (a) 0.1 and (b) 1.0 M GPEs.

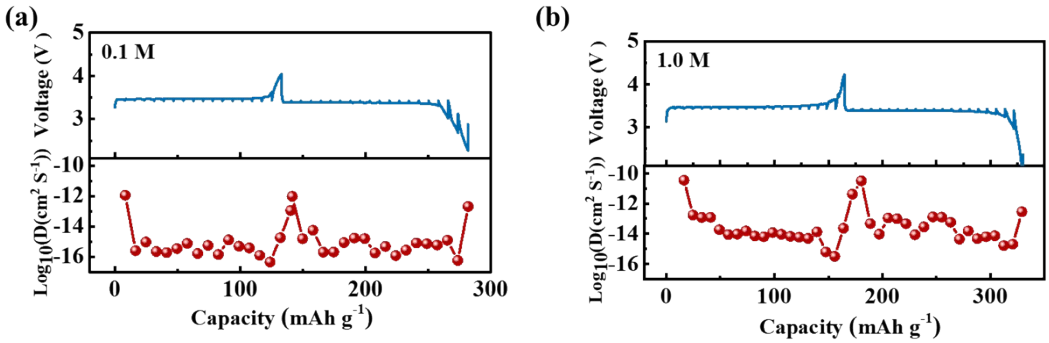

Figure S20 GITT curves of LFP electrodes and the calculated Li-ion diffusion coefficients tested at 25 °C using (a) 0.1 and (b) 1.0 M GPEs.

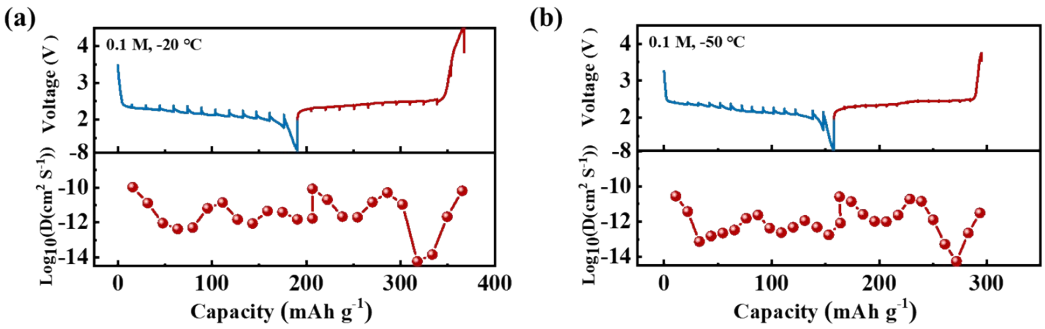

Figure S21 GITT curves of TAQB electrodes and the calculated Li-ion diffusion coefficients tested at (a) -20 °C and (b) -50 °C using 0.1 M GPE.

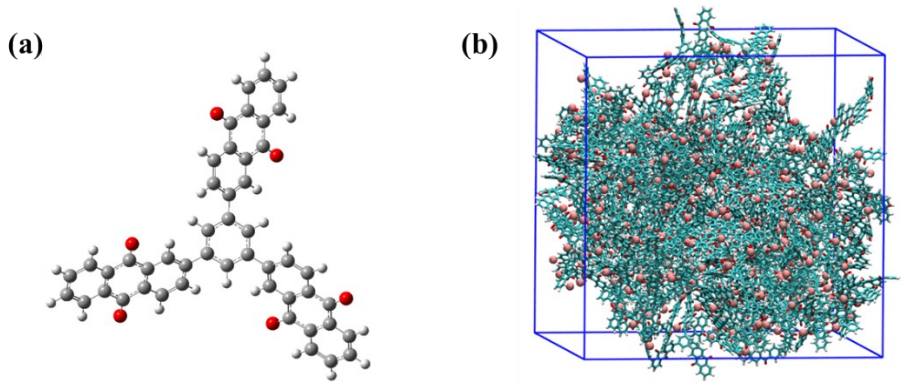

Figure S22 (a) Optimized structure of TAQB by DFT calculation and (b) snapshots obtained from MD simulations of the TAQB molecule complexed with two Li^+.

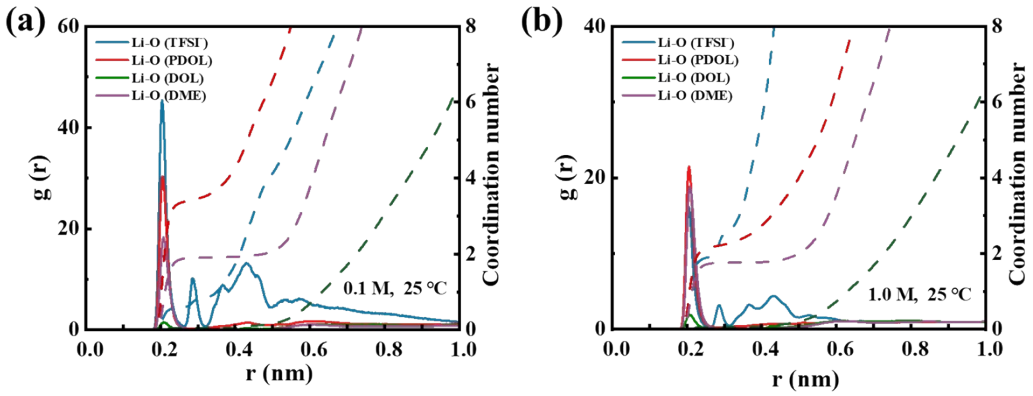

Figure S23 Radial distribution functions (RDF) and corresponding coordination numbers of (a) 0.1 and (b) 1.0 M GPEs at 25 °C.

As shown in **Figure S23**, within the first solvation shell (≤3 Å) of lithium ions, DOL molecules contribute minimally to Li^+ coordination, and the Li^+ solvation environment is primarily composed of PDOL, $TFSI^-$, and DME. Quantitative coordination analysis at 25 °C reveals that in 0.1 M GPE, each Li^+ is coordinated by an

average of 3.4 PDOL oxygens, 0.7 $TFSI^-$ oxygens, and 1.9 DME oxygens. Notably, increasing the electrolyte concentration to 1.0 M significantly decreased the coordination number of PDOL oxygens to 2.2, while that of $TFSI^-$ increased to 2.0.

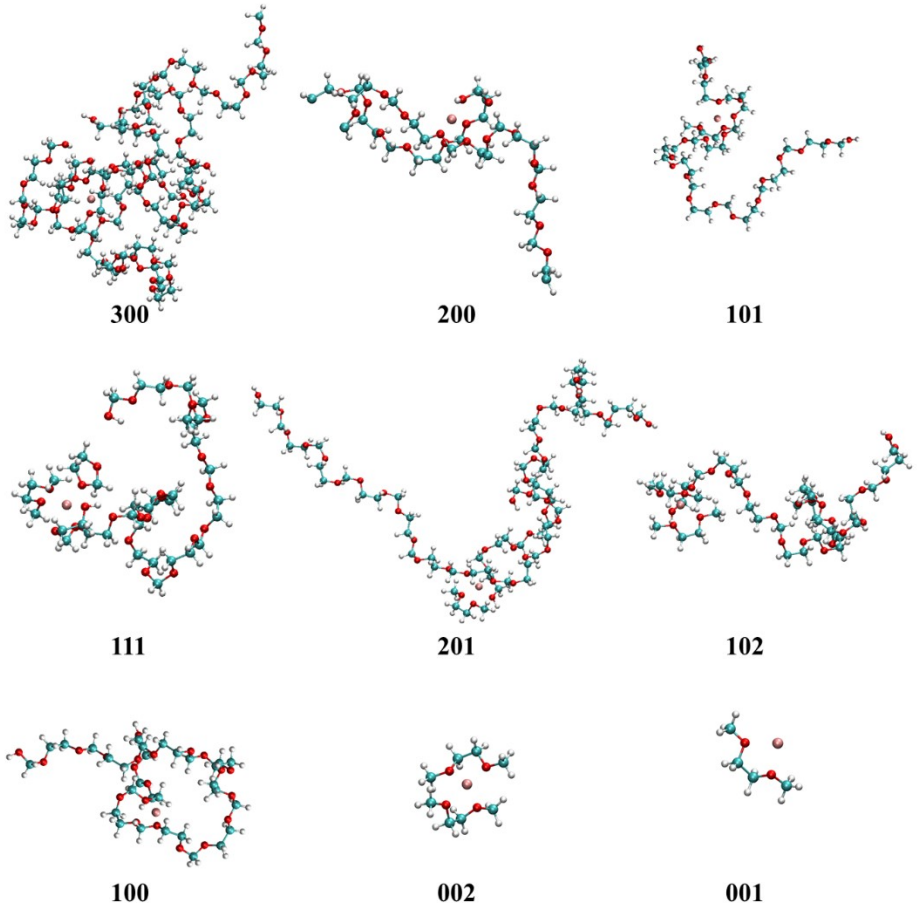

Figure S24 Partial Li^+ solvated structures in GPEs (here xyz represents one Li^+ with x PDOL, y DOL, and z DME around 0.3 nm).

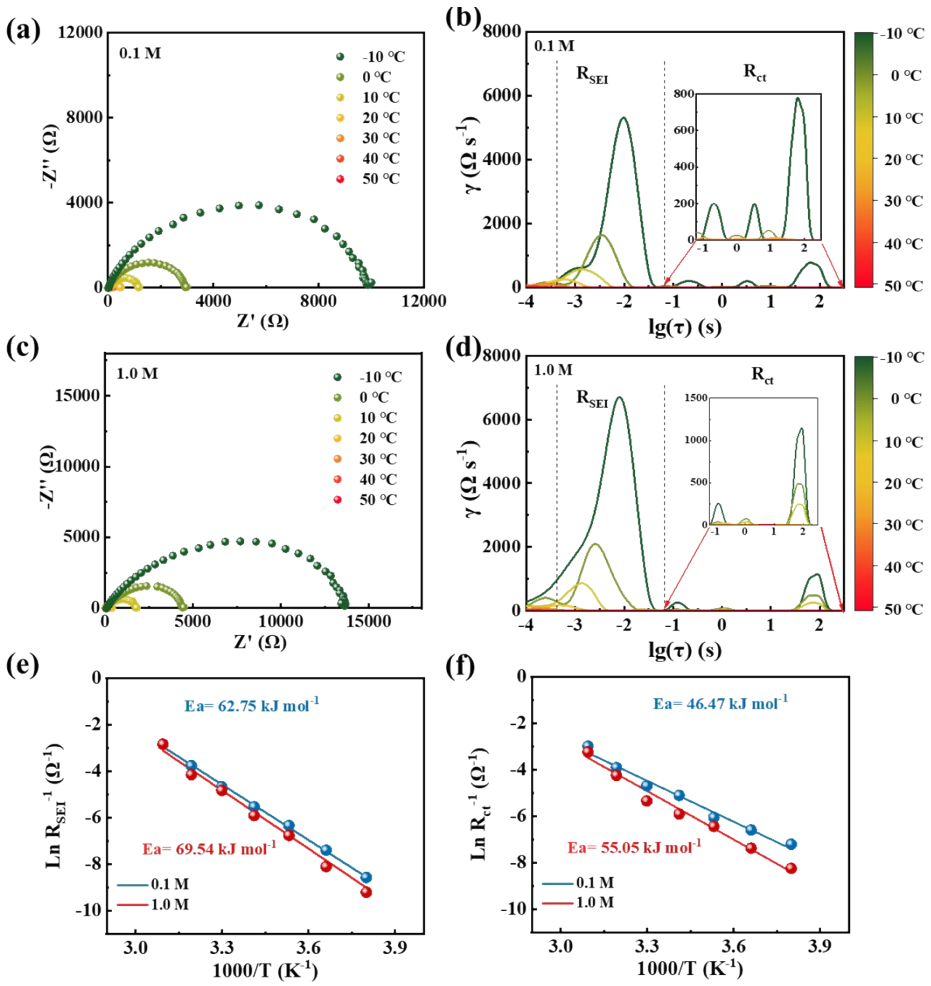

Figure S25. (a-d) EIS spectra and corresponding temperature-dependent DRT distributions of symmetrical Li cells with (a, b) 0.1 and (c, d) 1.0 M GPEs. The corresponding activation energy of (e) Li^+ transport through SEI and (f) Li^+ de-solvation.

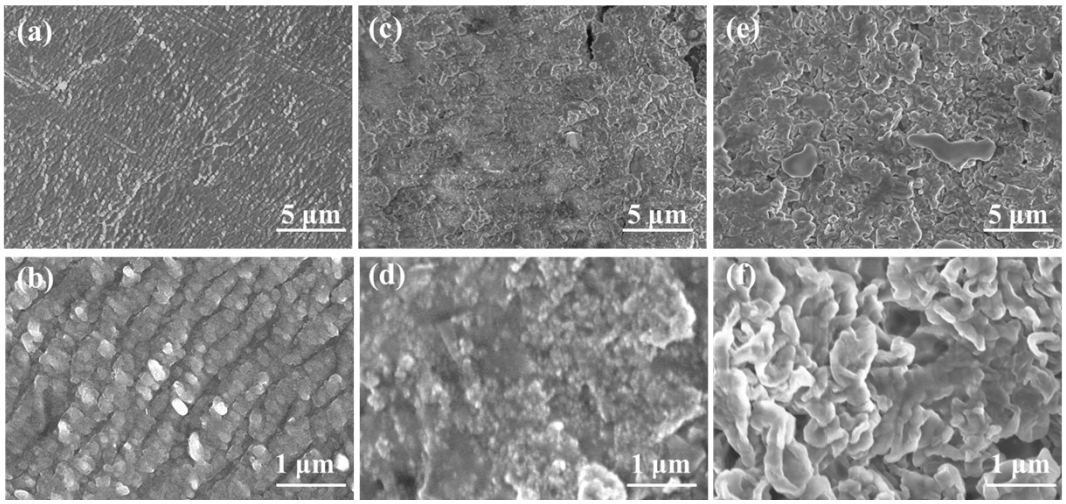

Figure S26. SEM images of the Li metal surface after 50 cycles of Li||Li symmetric cells operated at –50 °C with a current density of 1 mA cm^{-2} and an areal capacity of 1 mAh cm^{-2} using (a, b) 0.1, (c, d) 1.0 and (e, f) 3.0 M GPEs.

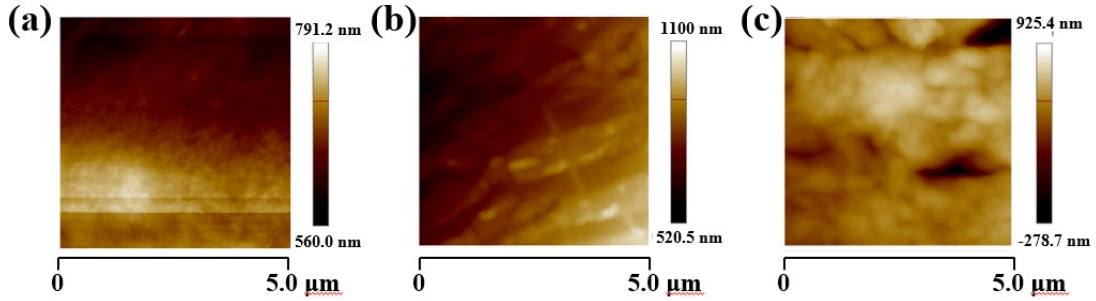

Figure S27. AFM scanning images of the Li metal surface after 50 cycles of Li||Li symmetric cells operated at –50 °C with a current density of 1 mA cm^{-2} and an areal capacity of 1 mAh cm^{-2} using (a) 0.1, (b) 1.0 and (c) 3.0 M GPEs.

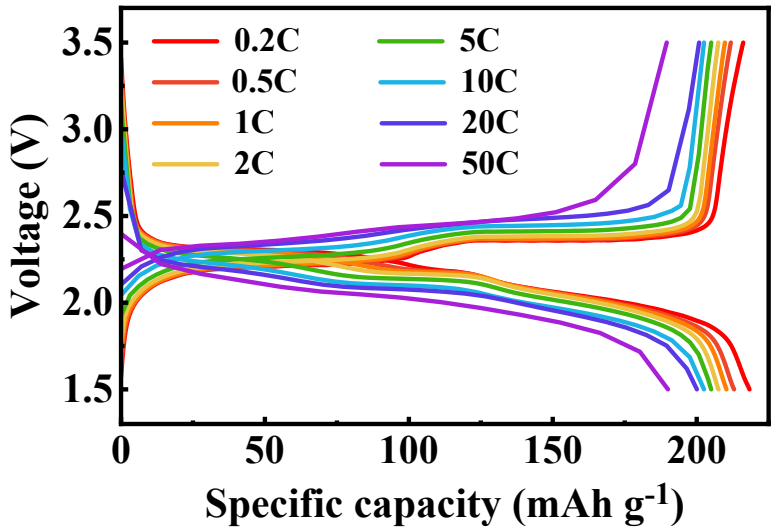

Figure S28. Charge–discharge curves of TAQB-Li battery using 0.1 M GPE with different current densities.

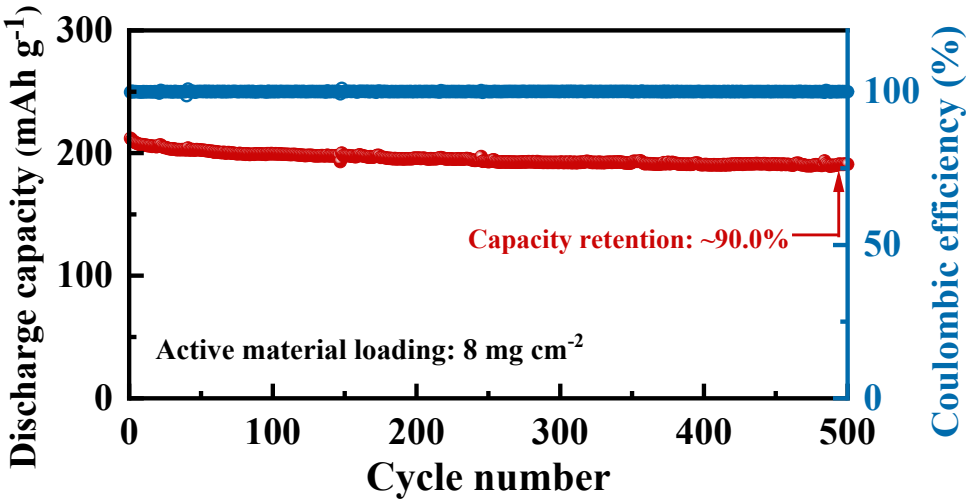

Figure S29. Cycling performance of TAQB-Li cells with a high active material loading of 8 mg cm^{-2} using 0.1 M GPE at 0.2 C.

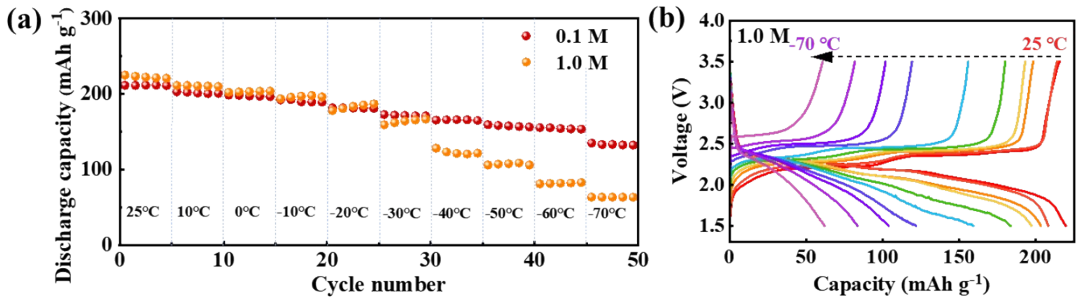

Figure S30. (a) Discharge capacity of TAQB-Li cells with 0.1 M and 1.0 M GPEs at different temperatures with a current density of 0.2 C and (b) the corresponding charge–discharge curves with 1.0 M GPE.

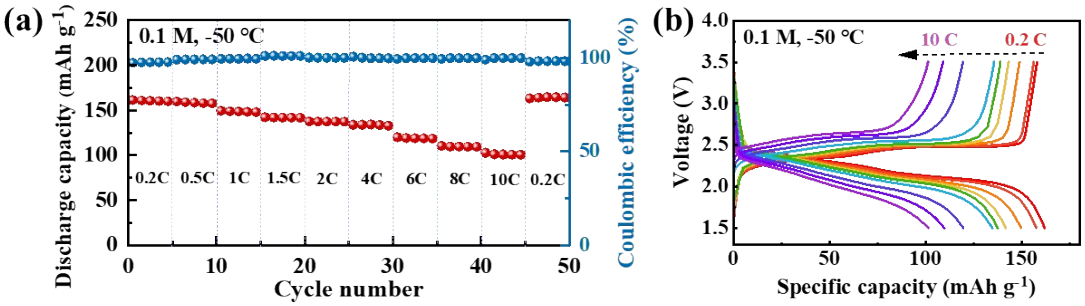

Figure S31. (a) Rate performance of TAQB-Li cells with 0.1 M GPE and (b) the corresponding charge–discharge curves at −50 °C.

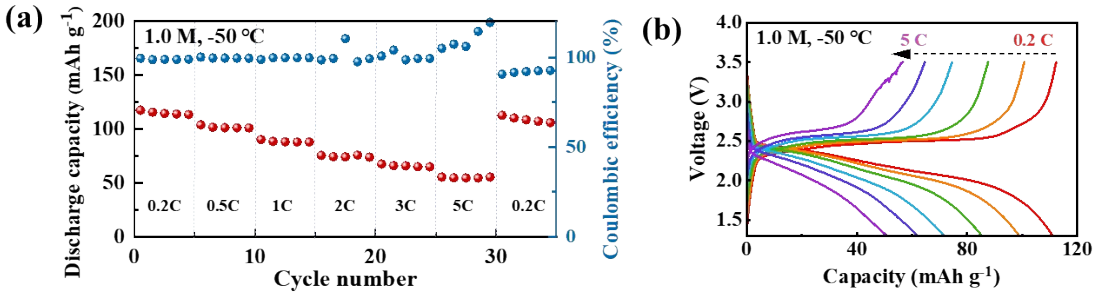

Figure S32. (a) Rate performance of TAQB-Li cells with 1.0 M GPE and (b) the corresponding charge–discharge curves at −50 °C.

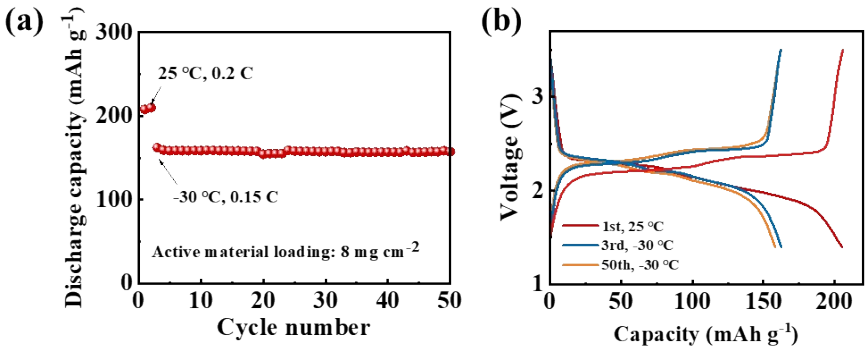

Figure S33. (a) Cycling performance of TAQB-Li cells with a high active material loading of 8 mg cm^{-2} using 0.1 M GPE at -30 °C and (b) the corresponding charge–discharge curves.

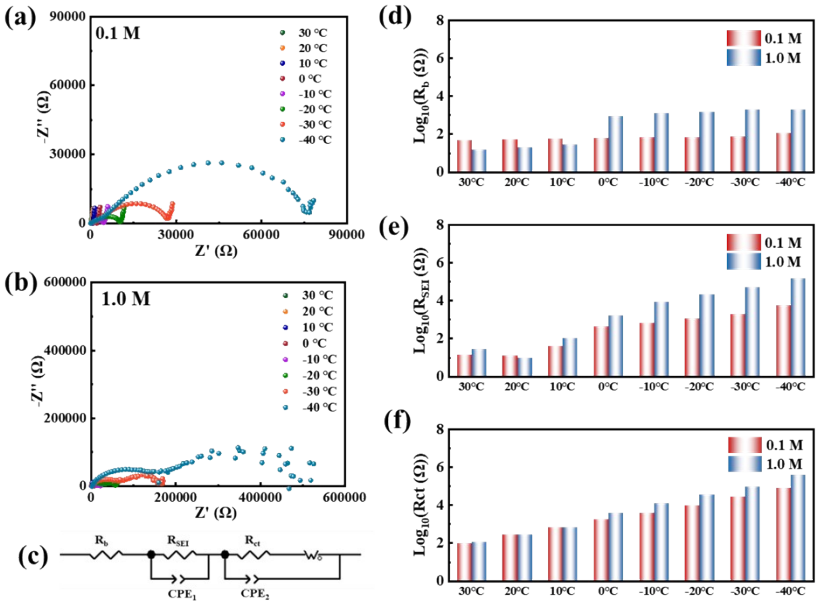

Figure S34. EIS changes of TAQB-Li cells under different working temperatures using GPEs with different LiTFSI concentrations of (a) 0.1 and (b) 1.0 M. (c) The corresponding equivalent circuit for fitting. Values of (d) the bulk resistance (R_b), (e) R_{SEI} and (f) R_{ct} under different working temperatures.

Table S1. The cost at different concentration in 1 dm^{-3} LiTFSI DOL-DME electrolyte.

Concentration (mol dm^{-3})	Weight of salt (g)	Weight of solvent (g)	Cost (CNY)
0.01	2.87	961.42	31.71
0.05	14.2	953.21	42.80
0.1	28.1	943.14	56.39
0.5	129.55	869.65	155.64
1.0	236.12	792.44	259.89
3.0	522.75	584.80	540.29

According to the quotation of the electrolyte company, we calculated the total cost of 1 dm^{-3} electrolyte. Wherein, the unit prices of DOL, DME and LiTFSI are 30, 30 and 1000 CNY kg^{-1} respectively. Obviously, the cost of low-concentration electrolytes is much lower than the high-concentration electrolytes.

Table S2 The electrochemical performance of TAQB-Li batteries using GPEs with different LiTFSI concentrations

Salte concentration (M)	Initial specific capacity (mAh g^{-1})	Capacity retention after 200 cycles
0.01 M	190	87%
0.05 M	202.8	82%
0.1 M	211.3	97%
1.0 M	215	95%
3.0 M	205.1	80%

Table S3 The electrochemical performance of LFP-Li batteries using GPEs with different LiTFSI concentrations

Salte concentration (M)	Initial specific capacity (mAh g^{-1})	Capacity retention after 200 cycles
0.1 M	147.2	77%
1.0 M	155	97%
3.0 M	91.8	Nearly 100%

Table S4. The Li-ion diffusion coefficients of the TAQB electrode with 0.1 and 1.0 M GPEs based on Randles-Sevick equation.

Electrolyte	Peak 1 (cm^2 s^{-1})	Peak 2 (cm^2 s^{-1})	Peak 3 (cm^2 s^{-1})	Peak 4 (cm^2 s^{-1})
0.1 M	1.2×10^{-10}	1.2×10^{-10}	1.4×10^{-10}	6.3×10^{-11}
1.0 M	1.7×10^{-10}	1.7×10^{-10}	1.2×10^{-10}	4.8×10^{-11}

Table S5. The Li-ion diffusion coefficients of the LFP electrode with 0.1 and 1.0 M GPEs based on Randles-Sevick equation.

Electrolyte	Peak 1 (cm^2 s^{-1})	Peak 2 (cm^2 s^{-1})
0.1 M	3.3×10^{-12}	3.1×10^{-12}
1.0 M	2.1×10^{-11}	1.5×10^{-11}

Table S6 A summary of various solvated structures and the corresponding de-solvation energies in 0.1 M GPE system

Solvated structure	223.15 K		298.15 K	
	Frequency (Hz)	De-solvation energy (kJ mol^{-1})	Frequency (Hz)	De-solvation energy (kJ mol^{-1})
300	123	453.2	110	445.7
200	299	463.5	231	458.8
101	103	459.5	116	451.2
111	102	469.8	95	461.4
001	44	358.3	60	350.3
201	157	376.8	182	371.9
102	153	468.1	152	454.2
003	51	498.3	51	490.6
002	51	474.8	42	463.3
Average		448.5		436.4

Note:
300 represents one Li ion with three PDOL, zero DOL, and zero DME around 0.3 nm,
101 represents one Li ion with one PDOL, zero DOL, and one DME around 0.3 nm,
111 represents one Li ion with one PDOL, one DOL, and one DME around 0.3 nm,
and so on.

Table S7 A summary of various solvated structures and the corresponding de-solvation energies in 1.0 M GPE system

Solvated structure	223.15 K		298.15 K	
	Frequency (Hz)	De-solvation energy (kJ mol^{-1})	Frequency (Hz)	De-solvation energy (kJ mol^{-1})
100	1138	529.5	1144	520.5
200	951	463.5	980	458.8
101	2548	459.5	2506	451.2
002	1202	474.8	1197	463.3
001	1276	358.3	1360	350.3
102	692	468.1	730	454.2
111	55	469.8	45	461.4

110	594	515.3	500	510.1
010	68	363.3	385	356.4
210	663	479.4	544	471.5
301	51	516.2	51	511.6
300	8	453.2	9	445.7
011	62	367.3	50	361.4
120	125	516.8	136	510.7
003	203	498.3	192	490.6
Average		462.7		449.6

Table S8 Electrochemical performance comparison of organic batteries in our work and the previous reports.

Electrolyte	Cathode/anode	Cycling stability at RT (capacity retention@cycle life)	Rate performance at LTs		Ref.
			Condition（rate, temperature）	LT vs. RT	
0.1M LiTFSI+ PDOL-based GPE	TAQB/Li	74%@2000	10C, -50℃	101mAh g^{-1} 50%	Our work
~1 M LiTFSI/EA in DCM (1/4, v/v)	PI/Li	69%@100	10C, -70 ℃	9 mAh g^{-1} 14%	[11]
1.8 M LiTFSI in EA	PTPAn/PNTCDA	83%@500	5C, -50 ℃	45 mAh g^{-1} 52%	[12]
1 M $LiFSI_{0.8}TFSI_{0.2}$ in HME/HEP (1/1, v/v)	PTCDA/Li	71%@200	0.1C, -40 ℃	75 mAh g^{-1} 57%	[13]
1 M $LiPF_6$ in EC/EMC (3/7, v/v)	PTO-2TH/Li	59%@4000	0.5C, 2 °C	141 mAh g^{-1} 49%	[14]
1 M LiFSI in BTFE/DME (5/1, v/v)	NCM811/Li	94%@200	0.2C, -40 °C	109 mAh g^{-1} 54%	[15]
1 M $LiPF_6$ in MTFP/FEC (9/1, v/v)	NCM811/Li	80%@250	0.1C, -50 °C	149 mAh g^{-1} 79%	[16]
2.5 M LiFSI in DPE/DIPE(1/1, v/v)	LFP/Li	84%@150	0.1C, -20 °C	92 mAh g^{-1} 59%	[17]
2.1 M LiTFSI in MTBE/THF (3/1, v/v)	LFP/Li	87%@1400	0.2C, -40 °C	106 mAh g^{-1} 69%	[18]
1.0 M LiDFOB in FEC/DMS/IF (4/7/9, v/v/v)	$LiCoO_2$/Li	95% @500	1/15C, -70 °C	120 mAh g^{-1} 60%	[19]
1.0 M LiFSI in DMM	$Li_4Ti_5O_{12}$/Li	77% @200	0.1C, -40 °C	100 mAh g^{-1} 60%	[20]

Reference

[1] M. Li, J. Yang, Y. Shi, Z. Chen, P. Bai, H. Su, P. Xiong, M. Cheng, J. Zhao, Y. Xu, *Adv. Mater.* **2022**, *34*, 2107226.

[2] J. Wang, R. M. Wolf, J. W. Caldwell, P. A. Kollman, D. A. Case, *J. Comput. Chem.* **2004**, *25*, 1157.

[3] C. I. Bayly, P. Cieplak, W. D. Cornell, P. A. Kollman, *J. Phys. Chem.* **1993**, *97*, 10269.

[4] B. Hess, C. Kutzner, D. Van Der Spoel, E. Lindahl, *J. Chem. Theory Comput.* **2008**, *4*, 435.

[5] H. J. C. Berendsen, J. P. M. Postma, W. F. Van Gunsteren, A. Dinola, J. R. Haak, *J. Chem. Phys.* **1984**, *81*, 3684.

[6] U. Essmann, L. Perera, M. L. Berkowitz, T. Darden, H. Lee, L. G. Pedersen, *J. Chem. Phys.* **1995**, *103*, 8577.

[7] L. G. Astrakas, C. Gousias, M. Tzaphlidou, *J. Appl. Phys.* **2012**, *111*, 074702.

[8] B. Hess, H. Bekker, H. J. C. Berendsen, J. G. E. M. Fraaije, *J. Comput. Chem.* **1997**, *18*, 1463.

[9] W. F. Van Gunsteren, H. J. C. Berendsen, *Mol. Simul.* **1988**, *1*, 173.

[10] K. Tang, X. Yu, J. Sun, H. Li, X. Huang, *Electrochim. Acta* **2011**, *56*, 4869.

[11] X. Dong, Y. Lin, P. Li, Y. Ma, J. Huang, D. Bin, Y. Wang, Y. Qi, Y. Xia, *Angew. Chem. Int. Ed.* **2019**, *58*, 5623.

[12] X. Dong, Z. Guo, Z. Guo, Y. Wang, Y. Xia, *Joule* **2018**, *2*, 902.

[13] M. Wang, T. Liu, X. Du, Y. Sun, L. Wang, Z. Zhang, X. Wang, G. Cui, *Energy Storage Mater.* **2023**, *60*, 102816.

[14] B. Ouyang, D. Huang, X. Bian, J. Guo, X. Peng, Y. Du, *Chem. Eng. J.* **2025**, *508*, 161004.

[15] J. Holoubek, K. Kim, Y. Yin, Z. Wu, H. Liu, M. Li, A. Chen, H. Gao, G. Cai, T. A. Pascal, P. Liu, Z. Chen, *Energy Environ. Sci.* **2022**, *15*, 1647.

[16] J. Holoubek, M. Yu, S. Yu, M. Li, Z. Wu, D. Xia, P. Bhaladhare, M. S. Gonzalez, T. A. Pascal, P. Liu, Z. Chen, *ACS Energy Lett.* **2020**, *5*, 1438−1447.

[17] H. Li, Y. Kang, W. Wei, C. Yan, X. Ma, H. Chen, *Nano-Micro Lett.* **2024**, *16*, 197.

[18] T. Liu, H. Li, J. Yue, J. Feng, M. Mao, X. Zhu, Y. sheng Hu, H. Li, X. Huang, L. Chen, L. Suo, *Angew. Chem. Int. Ed.* **2021**, *60*, 17547.

[19] J. Liu, B. Yuan, N. He, L. Dong, D. Chen, S. Zhong, Y. Ji, J. Han, C. Yang, Y. Liu, W. He, *Energy Environ. Sci.* **2023**, *16*, 1024.

[20] T. Ma, Y. Ni, Q. Wang, W. Zhang, S. Jin, S. Zheng, X. Yang, *Angew. Chem. Int. Ed.* **2022**, *61*, e202207927.